PAPER

CNT/Ni hybrid nanostructured arrays: synthesis and application as high-performance electrode materials for pseudocapacitors†

Jian Jiang,[ab] Jinping Liu,*[ab] Weiwei Zhou,[a] Jianhui Zhu,[b] Xintang Huang,[b] Xiaoying Qi,[c] Hua Zhang[c] and Ting Yu*[a]

CNT/Ni hybrid nanostructured arrays (NSAs) are synthesized on a stainless steel substrate through a one-step chemical-vapor-deposition (CVD) method using nullaginite NSAs as starting materials. During the CVD process, the nullaginite NSAs are transformed into Ni NSAs, which can further act as the catalysts to initiate the simultaneous *in situ* growth of CNTs on their surface, leading to an intriguing three-dimensional (3D) hybrid nanostructure. The resulting ordered CNT/Ni NSAs are highly porous and conductive, which are believed to be quite favorable for electrochemical applications. As a proof-of-concept demonstration of the functions of such a well-designed architecture in energy storage, the CNT/Ni NSAs are tested as the working electrodes of electrochemical capacitors (ECs). After being activated, the composite electrode exhibits both well-defined pseudo-capacitive and electrical double-layer behavior with high areal capacitance (up to $\sim$0.901 F cm^{-2}), excellent cyclability (nearly 100% capacitance retention after 5000 cycles), and outstanding rate capability. The unique interconnected hybrid structure and virtues inherited from the conductive CNT network and porous NSAs are believed to be responsible for the excellent performance.

1. Introduction

Electrochemical capacitors (ECs) have been greatly pursued in recent years due to their outstanding brilliances of longer life-span, better safety and faster charge–discharge capability compared with batteries.[1,2] Such unique advantages enable ECs to be good power supplies in hybrid electric or all-electric vehicles especially whenever high power densities are needed under certain circumstances, like acceleration, deceleration, or braking. Generally, ECs are classified into electrical double-layer capacitors (EDLCs) and pseudocapacitors based on distinct energy-storage principles.[3] The storage mechanism of EDLCs relies on the fast adsorption of ions onto the electrode surface; as a result, they are capable of offering a high power delivery ($\sim$10 kW kg^{-1}). However, limited by the accessible maximum of the electrochemically active surface area on electrode materials, the EDLCs usually deliver unsatisfactory energy density ($\sim$5 W h kg^{-1}).[4–6] Totally different from EDLCs based on the sole ion-adsorption

[a]Division of Physics and Applied Physics, School of Physical and Mathematical Sciences, Nanyang Technological University, 637371, Singapore. E-mail: yuting@ntu.edu.sg; Fax: +86-027-67861185
[b]Institute of Nanoscience and Nanotechnology, Department of Physics, Central China Normal University, Wuhan, 430079, Hubei, P.R. China. E-mail: liujp@phy.ccnu.edu.cn
[c]School of Materials Science and Engineering, Nanyang Technological University, 639798, Singapore
† Electronic supplementary information (ESI) available. See DOI: 10.1039/c1ee02293h

Broader context

Pseudocapacitors have been greatly pursued in recent years due to their advantages of high capacitance, good safety, superior rate capability to batteries and high energy density with respect to electric double-layer capacitors. However, they usually have to face formidable problems such as inferior electrical conductivity of pseudocapacitive materials, relatively poor ion transport kinetics and complicated electrode fabrication process. Hence, promising pseudocapacitors are expected to achieve the promotion of both electrical and ionic conductivity in solid electrodes and the optimization of electrode architecture design. To meet these demands, we hereby report an all-conductive hybrid nanostructure composed of Ni nanowall arrays and CNTs *in situ* built on the nanowall surface by a facile CVD method. After being electrochemically activated, the hybrid array inherits virtues from the conductive CNT network and porous Ni and exhibits both well-defined pseudo-capacitive and electrical double-layer behaviors with high areal capacitance, good cyclability, and outstanding rate capability.

mechanism, the pseudocapacitors behave more like batteries and store charges by reversible surface/near-surface Faradic reactions, either in the form of chemical adsorption/desorption of ions on the electrode surface, redox reactions with electrolyte, or doping/undoping of electrode materials.[7] Pseudocapacitive materials, such as conducting polymers and transition metal oxides/hydroxides including RuO_2, MnO_2, NiO, $Co(OH)_2$, $Ni(OH)_2$, *etc.*, can exhibit much higher energy density than EDLCs.[8,9]

Nevertheless, several issues still remain on the way to the development of pseudocapacitors, considering that their electrochemical performance is mainly dominated by two key factors: (i) electronic conduction in the electrode and (ii) ion transport in the electrode/electrolyte.[10] Firstly, most of the pseudocapacitive materials belong to wide band-gap semiconductors or even insulators;[11] with that, they usually exhibit poor electrical conductivity and bring about huge electronic resistance when serving as workhorse electrodes. This is quite detrimental to electron transfer and meanwhile possibly causes safety problems due to the generation of a large amount of joule heat during operation. Secondly, the bulk pseudocapacitive materials always suffer from poor ion transport kinetics.[12] Downsizing materials into the nanoscale and fabricating porous/mesoporous nanostructures can facilitate ions to enter into the inner side of the electrode matrix by offering sufficient ion-transport routes,[13] however, they in turn lead to the increase of electric resistance in the solid electrode due to increased boundaries. Thirdly, the traditional electrode fabrication requires both inactive and insulating polymer binders (like PVDF) and a pressing post-treatment (5–10 MPa). High-pressure treatment towards electrodes can indeed enhance the electrical contact and reduce the electrical resistance between active materials and current collector but causes a dense structure, which is unfavorable for the accessibility of electrolyte into active materials and fast diffusion rate of ions in the whole electrode matrix.[14,16c]

To address these issues and optimize the performance of pseudocapacitors, attempts on fabricating an electrode with both good electrical and ionic conductivity as well as searching for novel electrode design (binder and post-treatment free) are highly required.[15,16] In this article, we report on a designed electrode of CNT/Ni hybrid network nanostructured arrays (NSAs). The reason why we choose Ni-based materials is due to their good pseudocapacitive behavior and electrochemical stability, as demonstrated recently by many groups.[9] The as-designed electrodes have several highlights as follows: (i) both components in the electrode are electrically conductive. This can assure the ease of electron transfer within the electrode and from reaction sites to the conductive substrate, matching well with the requirement for high-power applications. (ii) The prepared CNT/Ni hybrid NSAs are very porous. The porous structures formed in Ni NSAs can effectively facilitate the ion transport into the solid electrode and meanwhile enhance the reaction surface area. In addition, compared with bulks, the nanoscale systems have exceptionally short ion-diffusion lengths and thus decrease the typical time for diffusion in solid materials. (iii) The synthesized CNT/Ni NSAs are well adhered to the current collector. This design confirms the quick direct electron transport to the conductive substrate; neither polymer binders nor conductive agents are needed. (iv) The entangled CNTs intimately connected to Ni NSAs can make

further contribution to the electrochemical capacitance while providing excellent conductivity.

It is noteworthy that the CNTs are grown straightforward on Ni NSAs by a CVD approach rather than introduced by mechanically mixing. The growth mechanism is proposed and confirmed by monitoring the whole fabrication process of CNT/Ni NSAs, as will be discussed later. As a proof-of-concept demonstration of its electrochemical behavior, we have measured the CNT/Ni hybrid NSAs as working electrodes for ECs. It is found that, after being electrochemically activated, the evolved hybrid electrode (CNT/NiOOH) exhibits a high areal capacitance (the maximum is up to ~0.901 F cm^{-2}), excellent cycling performance (no obvious capacitance loss after 5000 cycles) and good rate capability (80.1% capacitance retention at a large current density of 27.8 mA cm^{-2}).

2. Experimental section

2.1 Sample synthesis

Nullaginite NSAs were prepared using a facile hydrothermal method according to the previous literature[20] and employed as the precursor materials. A piece of clean stainless steel foil (30 × 10 × 0.2 mm^3) was immersed into a Teflon-lined stainless steel autoclave, in which there was a 50 mL homogeneous solution containing 1.24 g of $C_4H_6NiO_4 \cdot 4H_2O$, 1.5 g of $CO(NH_2)_2$ and 0.37 g of NH_4F. Then, the autoclave was sealed and left still in an electric oven at the temperature of 130 °C for 5 h. Until the equipment cooled down to room temperature, the sample was taken out, washed by distilled water several times and dried in an electric oven. Another tried precursor of Ni–Mn LDH NSAs was synthesized by a similar hydrothermal method. A 50 mL aqueous solution containing 0.169 g of $MnSO_4 \cdot H_2O$, 0.58 g of $Ni(NO_3)_2 \cdot 6H_2O$ and 0.7 g of $CO(NH_2)_2$ was transferred into a Teflon-lined stainless steel autoclave. Differently, a piece of clean Ti foil (30 × 10 × 0.3 mm^3) was immersed. The liner was sealed and maintained still at 125 °C for 6 h in an electric oven. After being cooled down, Ti foil with samples grown on was fetched out and cleaned. The typical synthesis of Ni NSAs and CNT/Ni hybrid NSAs was carried out in a horizontal, quartz tube-furnace system. A piece of substrate covered with nullaginite precursors was put in the centre of a quartz tube (tube diameter: 1 inch). Mixed EG and EA of 1 mL (volume ratio: 5 : 1) loaded in an alumina boat were placed at the upstream zone of the quartz tube (the distance from the alumina boat to the quartz-tube center: ~12 cm). Before heating, the quartz-tube reactor was sealed and flushed by Ar gas (200 sccm) for 20 min. For the synthesis of CNT/Ni hybrid NSAs, the furnace was heated to 920 K at a heating rate of ~15 K min^{-1} under a constant Ar flow of 130 sccm, held for 15 min and allowed to cool down to room temperature naturally. To prepare Ni NSAs, the furnace was only heated to 750 K and held for 1 min under the same conditions as described above.

2.2 Sample characterizations

The morphology and the crystalline structure of as-made products were characterized with a JEOL JSM-6700F field emission scanning electron microscope (FE-SEM) and a JEM 2010F high-resolution transmission electron microscope (HR-TEM). X-Ray

powder diffraction (XRD) patterns were recorded on a Bruker D8 Advance diffractometer using Cu Kα radiation. Raman spectroscopy (Witech CRM200, 532 nm) was used to characterize the products. The temperature was measured by a digital thermometer (Fluke, 52-II) with an accuracy of 1 K. The mass of electrode materials was measured on a microbalance with an accuracy of 0.01 mg (A&D Company N92, Japan).

2.3 Electrochemical measurements

Electrochemical measurements were performed on an electrochemical workstation (CHI 760D, CH Instruments Inc., Shanghai) using a three-electrode mode in 6 M KOH aqueous solution within the potential window of −0.2 to 0.52 V. The CNT/Ni hybrid or Ni NSAs (∼0.2 × 1.8 cm²; Ni NSA mass: ∼0.47 mg, CNT/Ni mass: ∼0.5 mg) was directly used as the working electrode. For comparison, the stainless steel substrate with a same area was also scanned under the same conditions (see Fig. S4†). The reference electrode and counter electrode were Ag/AgCl and platinum plate, respectively. Prior to electrochemical measurements, all the electrodes were sealed on all edges with epoxy resin except for the working surface area, and activated by additional 500 CV cycles (scanning rate: 50 mV s⁻¹). During the activated process, an electro-oxidation reaction is present on the Ni surface[26] as described below:

$$2Ni + O_2 + 2OH^- \rightarrow 2NiOOH$$

Areal and gravimetric capacitance were calculated by the equation below, respectively, where I is the constant discharge current, t is the discharging time, V is the voltage drop upon discharging (excluding the IR drop), m is the total mass of the active materials and S is the geometrical area of the electrode.

$$C_a = I \times t/(\Delta V \times S)$$

$$C_m = I \times t/(\Delta V \times m)$$

3. Result and discussion

3.1 Structure characterization, growth mechanism

Fig. 1a illustrates the schematic setup for the synthesis of CNT/Ni NSAs via a one-step CVD process conducted in a horizontal quartz-tube furnace. Rather than the hydrocarbons (ethylene, acetylene, etc.) commonly chosen as carbon sources for CNT growth, ethylene glycol (EG) mixed with ethanol (EA) (volume ratio: 5 : 1) was alternatively used as the carbon feedstock in our experiments. The interest in the EG/EA mixture is driven by its easy accessibility in the market, simplified operation (no need of heavy gas cylinders for hydrocarbon supply), low toxicity, and extremely low cost.[17] In a typical CVD synthesis, the EG/EA carbon source is evaporated at upstream and then transported to the high-temperature zone by Ar carrier gas, wherein the decomposition process occurs, leading to CNT growth on Ni NSAs which are evolved from nullaginite precursor's reduction. The detailed growth process will be proposed in the following discussion. A photograph of a severely bent sample shows no detachment of the as-grown materials (Fig. 1b), suggesting the
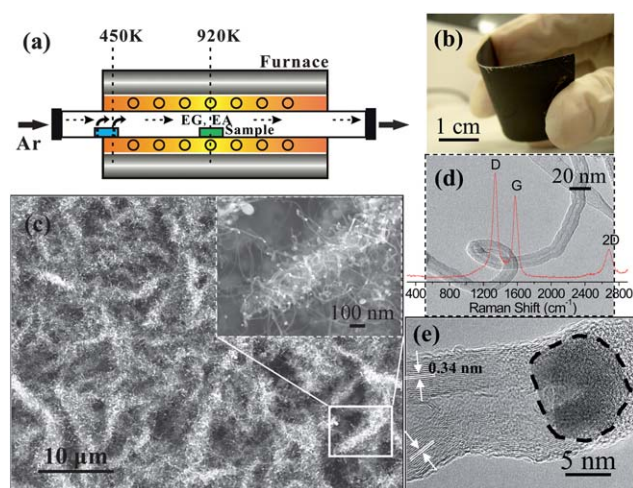

Fig. 1 (a) Schematic diagram for the synthesis of CNT/Ni NWAs on the stainless steel substrate via a CVD process conducted in a horizontal quartz-tube furnace. (b) Photograph of a severely bent CNT/Ni nanohybrid product. (c) Top-view SEM image of CNT/Ni NWAs. The inset is a typical zoom-in SEM image observation. (d) TEM and (e) HRTEM images of the as-made CNT/Ni composite. The inset is the Raman spectrum of the as-made product.

good adhesion and integrated capability of CNT/Ni NSAs. The scanning electron microscope (SEM) image shown in Fig. 1c signifies that the products possess a hierarchically three-dimensional (3D) hybrid nanostructure, consisting of one-dimensional (1D) CNTs "pillars" and two-dimensional (2D) nanowalls "foundation". The high-magnification SEM image reveals that a great number of entangled CNTs with typical length up to several hundreds of nanometres are epitaxially grown on the single nanowall surface. Moreover, as it can be seen, the as-formed hybrid products can preserve the profile of pristine arrayed morphology even after high-temperature reactions. Fig. 1d shows a typical transmission electron microscope (TEM) image of a single CNT pillar, evidencing that CNTs grown on Ni NSAs have intrinsic curly and tubular natures. A high-resolution TEM (HRTEM) image further reveals the multi-walled characteristic (with 10–20 layer sidewalls) and diameters (in the range of 15–25 nm) of the CNTs (Fig. 1e). The lattice spacing of 0.34 nm is in good agreement with the (006) interplanar spacing of the hexagonal carbon and in line with the XRD result, which will be presented in the later analysis. The Raman spectrum of final products is shown in the inset of Fig. 1d, where we can readily find the characteristic peaks of CNTs, involving G band (1578 cm⁻¹), D band (1340 cm⁻¹) and 2D band (2684 cm⁻¹).[18] As reported, the G band originates from the E_{2g} stretching mode of graphite, which is closely related to the vibration of sp² bonded carbon atoms in a 2D hexagonal lattice, while the D band reflects the graphite-structure imperfection.[19] In our spectrum, the intensity ratio of D to G band is calculated to be ∼1.1. The relatively high intensity of the D band indicates the existence of disordered carbon and structural defects. The imperfection is primarily attributed to the relative low-temperature ($T \leq 920$ K) CVD process compared with other reports ($T \approx 1100$ K);[4b] the lower reaction temperature could lead to insufficient pyrolysis of carbon sources and large quantities of chemical defects in or on CNTs. Nevertheless, from the perspective of electrochemical
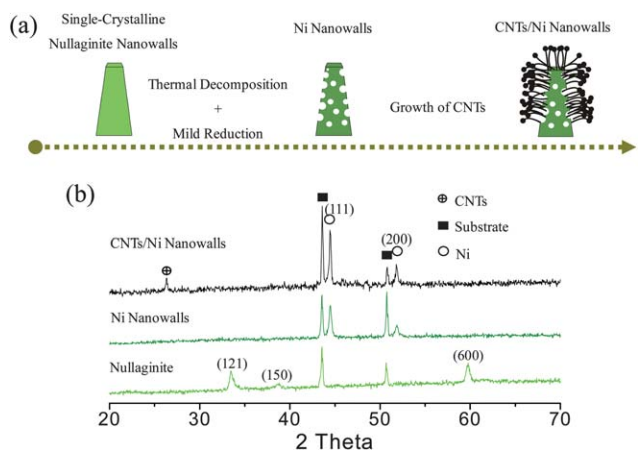
Fig. 2 (a) Schematic illustration of the preparation process of CNT/Ni NWAs on the stainless steel substrate. (b) XRD patterns of products obtained in the evolution stages.

applications, certain structural defects of CNTs, particularly in the form of oxygen functional groups (*e.g.* hydroxyl, epoxy, and carbonyl groups) on the CNT surface, are quite beneficial to improve the hydrophilicity of CNTs, thereby making electrodes achieve high specific capacitances in aqueous electrolytes.[4b]

The fabrication process of CNT/Ni NSAs with interesting 3D hierarchical structure is worth studying. On the basis of temperature-dependent experiments, the one-step CVD synthesis of CNT/Ni NSAs indeed comprises two chemical procedures. Fig. 2a shows the schematic illustration of the formation process of CNT/Ni NSAs on the stainless steel substrate. Seeking to monitor the whole growing process, the XRD patterns of samples obtained at different temperatures are also presented (Fig. 2b). In our case, single-crystalline nullaginite NSAs with robust mechanical contact to the supporting substrate were employed as precursors for the synthesis of CNT/Ni NSAs and prepared beforehand according to the previous work.[20] Diffraction peaks appearing at 2θ of 34.1°, 38.7° and 60° in the XRD pattern (Fig. 2b, bottom) are in good agreement with monoclinic nullaginite (JCPDS card no. 35-0501), corresponding to the facets of (121), (150) and (600), respectively. Fig. 3a displays a representative SEM image of nullaginite precursors,

revealing an integrated framework nanoarchitecture that is constructed by interconnected nanowall building blocks. The mean thickness of a single nanowall is ∼80 nm (Fig. 3b). TEM observation shows the nanowall unit possesses a plate-like geometrical shape and a smooth surface (Fig. S1a†). In the flow of fabrication procedures (Fig. 2a), the initial step is the evolution of Ni NSAs. The nullaginite precursor, one type of Ni-based carbonate salt, is believed to suffer from thermal decomposition and meanwhile undergo a gentle reduction when heated to 750 K. EG and EA play a prominent role in the reduction reactions on account of their unique alcoholysis or polyol process at high temperature.[21] Diffraction peaks located at 44.4° and 51.8° shown in Fig. 2b (middle) agree well with the standard diffraction pattern of Ni (JCPDS card no. 04-0850), proving the intermediate product has the signature of metallic Ni rather than NiO. Herein, we need to emphasize that, superior to strong reducing agents like H_2, EG and EA can offer a mild reduction procedure which can change the oxidation state and the structure at atomic scale whilst still maintain the framework topology on the mesoscale.[21] SEM images reflect that the as-made Ni metal nanostructured arrays can still keep the interconnected nanowall morphology just like the pristine arrayed architecture except the rough surface (Fig. 3c and d). The TEM image reveals that the morphology of the Ni nanowall is approximate to that of nullaginite nanoplates (Fig. S1b†). Besides, some roughness emerges on the nanowall surface, which is consistent with SEM observation. The as-formed Ni nanowalls are observed to have porous structures with a pore diameter in the range of 10–20 nm (inset in Fig. S1b†), the formation of which is presumably due to the removal of carbonate component. For comparison, we also tried the diluted H_2 (volume: 5%) as reducing agent to fabricate Ni NSAs following the same procedures. However, we cannot find any trace of nanowall structures maintained on the substrate except some disordered fused-like residuals (Fig. S2†). This implies that strong reducing agents are not alternative to EG/EA on making the arrayed metallic nanostructures. As the temperature increased up to 920 K, the pyrolysis of organics (EG/EA) took place and simultaneously launched the *in situ* growth of CNTs on Ni nanowalls. From the XRD pattern (Fig. 2b, top), it is easy to notice that, aside from peaks originating from Ni nanowalls and metal substrate, a new diffraction peak emerges at
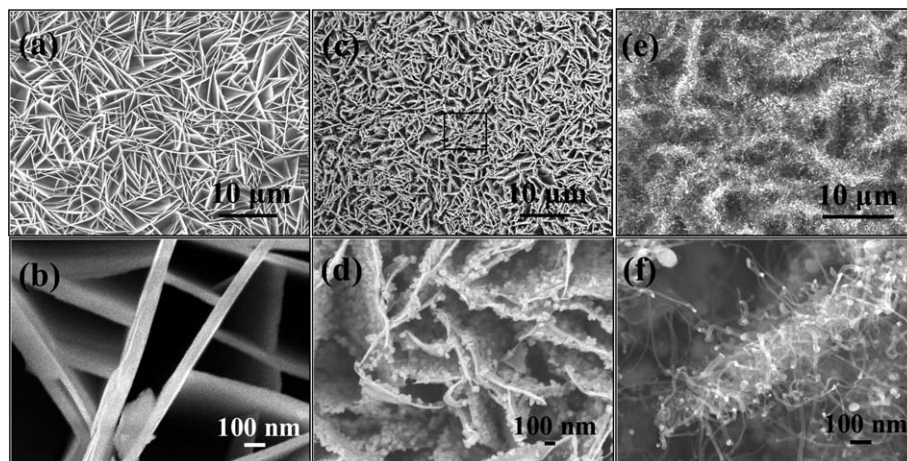

Fig. 3 SEM observations of the evolution of CNT/Ni hybrid NWAs.

2θ of 26.6°, which agrees well with the (006) facet of hexagonal carbon (JCPDS card no. 26-1076). This result confirms the presence of CNTs after the CVD process and is in strong agreement with previous HRTEM observation. Fig. 3e and f show the SEM images of final products, showing the as-formed CNTs are of high-purity (without any side-products of soot, or solid carbon) and uniformly grown on Ni nanowalls over a large area. TEM observation of the scraped CNT/Ni hybrid illustrates that the as-formed product has a loosely packed structure (Fig. S1c†), which could potentially increase the reacting sites and facilitate the ions transport into the solid electrode.

There is a highlight that the preparation of "CNTs-pillars-on-nanowall-foundation" hybrid structures does not stiffly depend on the choice of nullaginite as the initiating materials. In fact, we have tried another kind of material called Ni–Mn layered double hydroxides (LDH),[22] which also have arrayed nanowall morphology (see Fig. S3a and b†), to replace the nullaginite precursors. Fig. 4a presents a large-scale SEM observation of nanohybrids made from Ni–Mn LDH NSAs through the same CVD procedures. As shown, the hybrid products containing a mass of 2D evolved "mountain-like" structures are distributed on the supporting substrate (Ti foil), in the absence of any residual nanoparticle debris or dirt. Fig. 4b shows a SEM observation of the as-obtained "mountain" structures. It is obvious that there are plenty of nanofibres paved on "mountains" or other places. To get more close inspection to the nanostructures of the composite, a selected area in Fig. 4b is magnified, showing that the grown nanofibres with a soft and curly nature are highly entangled with each other (Fig. 4c). The as-obtained nanofibres are identified as MWCNTs through Raman (Fig. S4a†) and TEM characterizations (Fig. S4b†). In addition, the mean thickness of the as-made film product is determined to be around 4 μm from a representative cross-sectional SEM image (Fig. 4d). The above results show that our protocol can be readily extended to prepare other desired nanocomposites by simply choosing different catalyst-containing nanowalls as the scaffold.
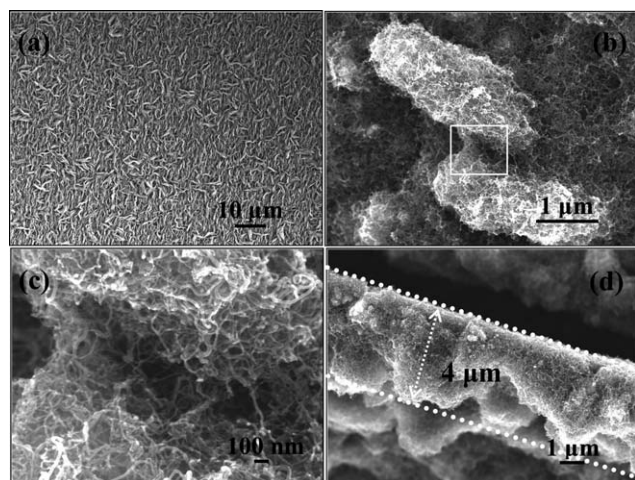
3.2 Application as pseudocapacitive materials

In our case, CNT/Ni NSAs are purposely designed and applied as ideal additive-free pseudocapacitive electrodes because they are conductive, full of nanosized pores and grown on the current collector. To highlight the electrochemical superiority of the CNT/Ni NSAs, pure Ni NSAs and bulky Ni foil are also studied for comparison. The electrochemical tests were carried out in a three-electrode configuration with a Pt plate counter-electrode and a saturated Ag/AgCl reference electrode in 6 M KOH aqueous electrolyte. Fig. 5 successively presents the cyclic voltammograms (CVs) of the activated bulky Ni foil, Ni NSAs, and CNT/Ni NSA electrodes at a constant scan rate of 50 mV s⁻¹. A pair of symmetric cathodic and anodic peaks can be clearly observed on each CV curve in a potential range of −0.2 to 0.52 V, implying the presence of reversible faradic reactions and pseudo-capacitive behavior of all tested samples. Previous studies have assured the electrochemical behavior is associated with the reversible faradic process, which can be described as follows:[9]

$$NiOOH + H_2O + e^- \leftrightarrow Ni(OH)_2 + OH^-$$
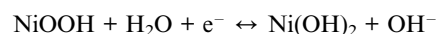
where NiOOH is generated from the electrochemical activated process.[26] The XRD test (Fig. S6a†) and Raman spectrum analysis (Fig. S6b†) have been conducted towards activated samples (Ni NSAs) to confirm the presence of the electrochemical activation process. In the XRD pattern, two broad amorphous peaks centered at 18.3° and 34.5° are well indexed to the β-NiOOH, which is well consistent with the previous result[27] and evidences the appearance of NiOOH after the electrochemical activation. The Raman spectrum shows a couple of peaks at 475 and 565 cm⁻¹ attributed to the typical stretching vibrational modes of [Ni^{III}=O] and [Ni^{III}–O$^{(-)}$], respectively,[28] further confirming the electrochemical conversion from Ni to Ni^{III}–OOH.[26b] As is known, the average specific capacitance of different samples (per cm²) can be roughly estimated from the areas surrounding by the CVs. In the case of Ni foil, the extremely small integrated area of CV obviously suggests the bulky Ni in an alkaline electrolyte possesses a negligible pseudo-capacitance. By contrast, the CVs of Ni nanosized products show much larger areas than that of bulk Ni foil. The greatly enhanced capacitance could be ascribed to the increased electrode surface
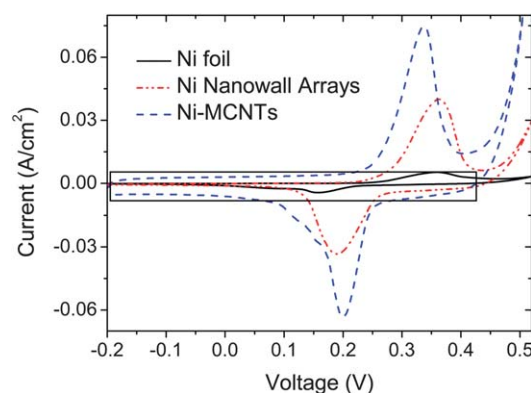

Fig. 4 (a) Large-area, (b and c) localized and (d) cross-sectional SEM observations of CNTs-on-nanowall hybrids evolved from Ni–Mn LDH precursors. The region enclosed in the box in (b) is magnified and shown in (c).

Fig. 5 CV curve of activated bulky Ni foil, Ni NSAs and CNT/Ni NSA electrodes in a potential range of −0.2 to 0.52 V at a constant scanning rate of 50 mV s⁻¹.

area and the decreased reaction energy barrier for nano-materials.[23] It is noteworthy that the CNT/Ni NSA electrode shows distinct capacitive behavior in comparison with Ni NSAs and Ni foil. Specifically, the peak current value of CNT/Ni NSAs is the highest, which indicates the hybrid of CNT/Ni has the strongest capacitive behavior. In addition, it is visible that at the same scan rate the peak separation for CNT/Ni NSAs is quite less than that of Ni NSAs and Ni foil. This suggests the CNT/Ni NSA electrode has a better electron transfer capability.[25] Moreover, the CV of CNT/Ni NSAs expands and becomes approximately rectangular in the marked region. The difference in CV shape and simultaneously increased integrated area should certainly be attributed to the presence of CNTs, which can store electric energy by following the electric double-layer mechanism.

The galvanostatic charge/discharge tests of different samples have been conducted at various current densities in the potential window between -0.1 V and 0.4 V under ambient atmosphere. The charge/discharge curves have been recorded, as displayed in Fig. 6. The maxima of discharge areal capacitances of CNT/Ni NSAs, Ni NSAs, and Ni foil are measured to be ${\sim}0.901$ F cm^{-2} (at 0.69 mA cm^{-2}), ${\sim}0.477$ F cm^{-2} (at 0.83 mA cm^{-2}), and ${\sim}0.056$ F cm^{-2} (at 0.42 mA cm^{-2}), respectively. We further compare their electrochemical performance at the same discharging rate. At a rate of ${\sim}1$ mA cm^{-2}, the measured capacitance of CNT/Ni NSAs is around 0.879 F cm^{-2} (621 F g^{-1}), which is 2.06 times of that of Ni NSAs (0.426 F cm^{-2}; 301 F g^{-1}), and over 18 times higher than that of Ni foil (0.048 F cm^{-2}; 33.9 F g^{-1}). This result illustrates that both electrodes of nanosized Ni are capable of delivering areal capacitance far more than bulk Ni foil. Meanwhile, CNT/Ni NSAs have apparently exceeded Ni NSAs in the capacitive performance. To account for the reason, it is believed that the "velvet-like" CNTs built on Ni nanowalls can reversibly adsorb ions on their surfaces, forming the EDLC and contributing to the total capacitance. Apart from that, the CNT/Ni hybrids have a loosely packed and porous structure. As a result, more reaction sites would appear on the electrode, leading to the accessibility of higher pseudo-capacitance per unit area. Fig. 6d further illustrates the relationship between the increased current density and the areal pseudo-capacitance for the three samples. Within the whole current density range, both electrodes of nanosized Ni show outstanding rate performance and much larger capacitance than bulky Ni. When tested at the highest rate of 27.2 mA cm^{-2} (22.3 A g^{-1}), the CNT/Ni NSA electrode can still deliver a large capacitance of 0.722 F cm^{-2} (${\sim}514$ F g^{-1}), which is maintained up to 80.1% of that at 0.694 mA cm^{-2}. The Ni NSA electrode also reaches a high capacitance of 0.304 F cm^{-2} (${\sim}213$ F g^{-1}) at 27.2 mA cm^{-2} (${\sim}23$ A g^{-1}), nearly 63.7% of its maximum measured at ${\sim}0.8$ mA cm^{-2} (${\sim}0.63$ A g^{-1}). Strikingly, these values are even much higher than the capacitance of Ni foil tested at a lowest current rate (${\sim}0.42$ mA cm^{-2}; 0.37 A g^{-1}). Besides, along with progressively increased charge–discharge rate, the CNT/Ni NSA electrode exhibits a better capacitive maintenance capability (80.1%) than pure Ni NSAs (63.7%). We propose that the superior electrochemical behavior can be attributed to the unique hybrid architecture and possibly synergistic effects resulting from the great ionic conductivity offered by porous nanowall networks and good electrical conductivity aided by entangled CNTs on their surface.[24] CNTs are highly entangled with each other and solidly paved on the Ni nanowall surface. This forms a mechanically robust conductive network structure, which is propitious to quick electron transfer and strengthen the porous nanowalls.

To highlight the superior electrochemical performance of hybrid CNT/Ni NSA electrodes, cycling response up to 5000 times was recorded at the programmed current density, as shown in Fig. 7. The CNT/Ni NSA electrode was initially subjected to a continuous cycling for 1000 times at 2.78 mA cm^{-2} (2.42 A g^{-1}), in this case, it delivered a mean capacitance of ${\sim}0.865$ F cm^{-2}
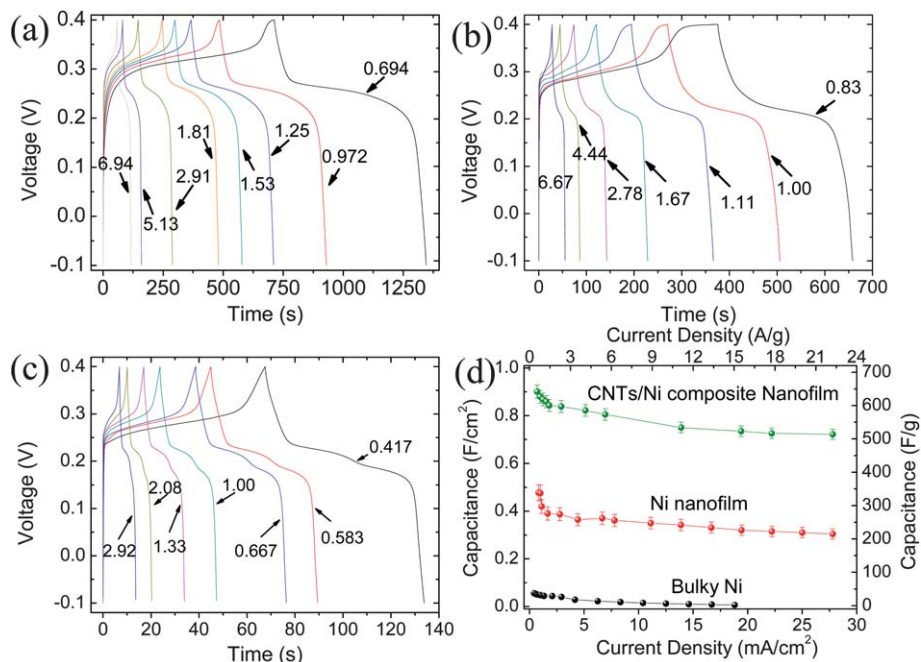

Fig. 6 Charge/discharge curves for (a) CNT/Ni NSAs, (b) Ni NSAs and (c) Ni foil in the potential window of -0.1 to 0.4 V at various current densities. The units for current density (indicated by arrow) are mA cm^{-2}. (d) Current density dependence of the areal capacitance for the three electrodes.
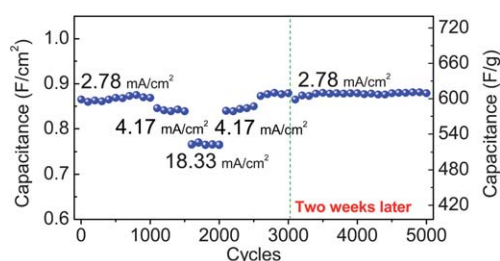
Fig. 7 Cycling response (5000 cycles) of CNT/Ni NSAs at progressively varied current density.

($\sim$601 F g^{-1}) without noticeable decrease. During the following 2000 cycles, the electrode was measured at 4.17 mA cm^{-2} (3.62 A g^{-1}), 18.33 mA cm^{-2} (15.9 A g^{-1}), and 4.17 mA cm^{-2} (3.62 A g^{-1}), successively. The stepwise testing reveals the electrode of CNT/Ni NSA could still remain electrochemically stable even after suffering from sudden current changes. Furthermore, upon switching the current density back to 2.78 mA cm^{-2} (2.42 A g^{-1}), the capacitance of CNT/Ni NSAs ($\sim$0.87 F cm^{-2}; $\sim$604.5 F g^{-1}) was able to be fully recovered, demonstrating the brilliant capacity retention of this hybrid. In order to examine the endurable capability of the tested electrode, we purposely power off the electrochemical workstation, kept the electrode still in the electrolyte for two weeks, and then let it go on with the test lasting for another 2000 cycles under the same rate (2.78 mA cm^{-2}; 2.42 A g^{-1}). It was found that the CNT/Ni NSA electrode can reflect excellent electrochemical endurability, good electrochemical stability as well as long-term cyclic lifetime, as evidenced by its good capacitance retention (no obvious capacitance loss).

Conclusions

In summary, we report a methodology of fabricating CNT/Ni NSAs on a stainless steel substrate by using nullaginite NSAs as the starting materials. The formation mechanism has been put forward based on the monitoring of the entire fabrication process. Porous Ni NSAs are initially evolved from the nullaginite precursors followed by *in situ* CNT growth on Ni NSAs *via* a CVD process, forming an interesting "CNTs pillars-on-nanowall foundation" hybrid structure. The electrode design concept can be readily extended by selecting other Ni-containing hydroxides as precursors. Moreover, when activated, CNT/Ni hybrid NSAs can be used as high-performance electrode materials for ECs. They display well-defined pseudocapacitive capabilities with a high areal capacitance and good rate capability. The improvement could be ascribed to the hybrid nanostructure as well as a synergetic effect between CNTs and NSAs, which will be promising for a large spectrum of device applications.

Acknowledgements

References and notes

1 (a) P. Simon and Y. Gogotsi, *Nat. Mater.*, 2008, **7**, 845; (b) D. Pech, M. Brunet, H. Durou, P. Huang, V. Mochalin, Y. Gogotsi, P. Taberna and P. Simon, *Nat. Nanotechnol.*, 2010, **5**, 651; (c) C. Yu, C. Masarapu, J. Rong, B. Wei and H. Jiang, *Adv. Mater.*, 2009, **21**, 4793.

2 (a) M. Kaempgen, C. K. Chan, J. Ma, Y. Cui and G. Gruner, *Nano Lett.*, 2009, **9**, 1872; (b) J.-H. Kim, K. Zhu, Y. F. Yan, C. L. Perkins and A. Frank, *Nano Lett.*, 2010, **10**, 4099; (c) W. Zhou, J. Liu, T. Chen, K. Tan, X. Jia, Z. Luo, C. Cong, H. Yang, C. Li and T. Yu, *Phys. Chem. Chem. Phys.*, 2011, **13**, 14462.

3 (a) J. Liu, G. Z. Cao, Z. G. Yang, D. H. Wang, D. Dubois, X. D. Zhou, G. L. Graff, L. R. Pederson and J. G. Zhang, *ChemSusChem*, 2008, **1**, 676; (b) P. J. Hall, M. Mirzaeian, S. I. Fletcher, F. B. Sillars, A. J. R. Rennie, G. O. Shitta-Bey, G. Wilson, A. Crudenb and R. Carter, *Energy Environ. Sci.*, 2010, **3**, 1238.

4 (a) E. Raymundo-Pinero, M. Cadek and F. Beguin, *Adv. Funct. Mater.*, 2009, **19**, 1032; (b) H. Zhang, G. P. Cao and Y. S. Yang, *Energy Environ. Sci.*, 2009, **2**, 932.

5 (a) Y. Zhu, S. Murali, M. Stoller, K. Ganesh, W. Cai, P. Ferreira, A. Pirkle, R. Wallace, K. Cychosz, M. Thommes, D. Su, E. Stach and R. Ruoff, *Science*, 2011, **332**, 1537; (b) Z. Luo, T. Yu, J. Shang, Y. Wang, S. Lim, L. Liu, G. Gurzadyan, Z. Shen and J. Lin, *Adv. Funct. Mater.*, 2009, **19**, 1032; (c) H. Itoi, H. Nishihara, T. Kogure and T. Kyotani, *J. Am. Chem. Soc.*, 2011, **133**, 1165.

6 C. Z. Yuan, B. Gao, L. F. Shen, S. D. Yang, L. Hao, X. J. Lu, F. Zhang, L. J. Zhang and X. G. Zhang, *Nanoscale*, 2011, **3**, 529.

7 M. Winter and R. J. Brodd, *Chem. Rev.*, 2004, **104**, 4245.

8 (a) H. Zhang, G. P. Cao, Z. Y. Wang, Y. S. Yang, Z. J. Shi and Z. N. Gu, *Nano Lett.*, 2008, **8**, 2664; (b) J. P. Liu, J. Jiang, C. W. Cheng, H. X. Li, J. X. Zhang, H. Gong and H. J. Fan, *Adv. Mater.*, 2011, **23**, 2076; (c) L. Cao, F. Xu, Y. Y. Liang and H. L. Li, *Adv. Mater.*, 2004, **16**, 1853.

9 (a) H. L. Wang, H. S. Casalongue, Y. Y. Liang and H. J. Dai, *J. Am. Chem. Soc.*, 2010, **132**, 7472; (b) J. P. Liu, C. W. Cheng, W. W. Zhou, H. X. Li and H. J. Fan, *Chem. Commun.*, 2011, **47**, 3436; (c) T. Y. Wei, C. H. Chen, H. C. Chien, S. Y. Lu and C. C. Hu, *Adv. Mater.*, 2010, **22**, 347; (d) J. W. Lang, L. B. Kong, W. J. Wu, Y. C. Luo and L. Kang, *Chem. Commun.*, 2008, 4213.

10 H. G. Zhang, X. D. Yu and P. V. Braun, *Nat. Nanotechnol.*, 2011, **6**, 277.

11 (a) Y. G. Li, B. Tan and Y. Y. Wu, *Nano Lett.*, 2008, **8**, 265; (b) C. Guan, J. Liu, C. Cheng, H. Li, X. Li, W. Zhou, H. Zhang and H. J. Fan, *Energy Environ. Sci.*, 2011, DOI: 10.1039/c1ee01685g; (c) J. Jiang, J. P. Liu, R. M. Ding, J. H. Zhu, Y. Y. Li, A. Z. Hu, X. Li and X. T. Huang, *ACS Appl. Mater. Interfaces*, 2011, **3**, 99.

12 N. Ergang, J. Lytle, K. Lee, S. Oh, W. Smyrl and A. Stein, *Adv. Mater.*, 2006, **18**, 1750.

13 J. Sakamoto and B. Dunn, *J. Mater. Chem.*, 2002, **12**, 2859.

14 W. W. Zhou, C. W. Cheng, J. P. Liu, Y. Y. Tay, J. Jiang, X. T. Jia, J. X. Zhang, H. Gong, H. H. Hng, T. Yu and H. J. Fan, *Adv. Funct. Mater.*, 2011, **21**, 2439.

15 C. Ban, Z. Wu, D. T. Gillaspie, L. Chen, Y. Yan, J. L. Blackburn and A. C. Dillon, *Adv. Mater.*, 2010, **22**, E145.

16 (a) H. Kim, M. Seo, M. H. Park and J. Cho, *Angew. Chem., Int. Ed.*, 2010, **49**, 2146; (b) U. Kasavajjula, C. S. Wang and A. J. Appleby, *J. Power Sources*, 2007, **163**, 1003; (c) J. Jiang, Y. Y. Li, J. P. Liu and X. T. Huang, *Nanoscale*, 2011, **3**, 45.

17 S. Maruyama, R. Kojima, Y. Miyauchi, S. Chiashi and M. Kohno, *Chem. Phys. Lett.*, 2002, **360**, 229.

18 Z. Chen, W. Ren, L. Gao, B. Liu, S. Pei and H. Cheng, *Nat. Mater.*, 2011, **10**, 424.

19 R. Yuge, J. Miyawaki, T. Ichihashi, S. Kuroshima, T. Yoshitake, T. Ohkawa, Y. Aoki, S. Iijima and M. Yudasaka, *ACS Nano*, 2010, **4**, 7337.

20 J. H. Zhu, J. Jiang, J. P. Liu, R. M. Ding, H. Ding, Y. M. Feng, G. M. Wei and X. T. Huang, *J. Solid State Chem.*, 2011, **184**, 578.

21 H. Tuysuz, Y. Liu, C. Weidenthaler and F. Schuth, *J. Am. Chem. Soc.*, 2008, **130**, 14108.

22 (a) Q. Zhang, M. Zhao, D. Tang, F. Li, J. Huang, B. Liu, W. Zhu, Y. Zhang and F. Wei, *Angew. Chem., Int. Ed.*, 2010, **49**, 1; (b) F. Kovanda, T. Grygar and V. Dornicak, *Solid State Sci.*, 2003, **5**, 1091.

23 (a) M. Shaijumon, E. Perre, B. Daffos, P. Taberna, J. Tarascon and P. Simon, *Adv. Mater.*, 2010, **22**, 4978; (b) G. Ouyang, C. X. Wang and G. W. Yang, *Chem. Rev.*, 2009, **109**, 4221.

24 (*a*) M. S. Wu, C. Y. Huang and K. H. Lin, *Electrochem. Solid-State Lett.*, 2009, **12**, A129; (*b*) Y. Wang, L. Yu and Y. Xia, *J. Electrochem. Soc.*, 2006, **153**, A743–A748; (*c*) Q. Song, G. Aravindaraj, H. Sultana and S. Chan, *Electrochim. Acta*, 2007, **53**, 1890.

25 R. S. Nicholson, *Anal. Chem.*, 1965, **37**, 1351.

26 (*a*) S. L. Yau, F. F. Fan, T. P. Moffat and A. J. Bard, *J. Phys. Chem.*, 1994, **98**, 5493; (*b*) A. S. Adekunle and K. I. Ozoemena, *Electrochim. Acta*, 2008, **53**, 5774.

27 D. Singh, *J. Electrochem. Soc.*, 1998, **145**, 116.

28 S. Deabate, F. Fourgeot and F. Henn, *Electrochim. Acta*, 2006, **51**, 5430.